Fall 2017

Diffusion and mechanical characterization of nanoparticle-enabled diffusion controlled materials

Joseph Louis Volpe

Department:

DIFFUSION AND MECHANICAL CHARACTERIZATION OF NANOPARTICLE-ENABLED DIFFUSION CONTROLLED MATERIALS

by

JOSEPH LOUIS VOLPE

A THESIS

Presented to the Graduate Faculty of the

MISSOURI UNIVERSITY OF SCIENCE AND TECHNOLOGY

In Partial Fulfillment of the Requirements for the Degree

MASTER OF SCIENCE

in

MECHANICAL ENGINEERING

2017

Approved by

Lianyi Chen, Advisor
Charles Wojnar
Frank Liou

PUBLICATION THESIS OPTION

This thesis consists of the following two articles which will be submitted for publication as follows:

Paper I: Pages 11-21 are intended for submission to Scripta Materialia.

Paper II: Pages 22-29 are intended for submission to Scripta Materialia.

ABSTRACT

Nanoparticle-enabled diffusion control has been shown to rapidly refine multiphase microstructures during slowly cooled casting. This thesis characterizes the diffusion and the mechanical properties of nanoparticle-enabled diffusion controlled materials. To characterize diffusion properties, *in-situ* characterization is performed to verify the nanoparticle-enabled diffusion control mechanism. Materials with nanoparticles were observed to decrease the diffusion coefficient by at least one order of magnitude under similar melting conditions as compared to materials without nanoparticles. To understand mechanical properties, the nanoparticles that assembled at the growing interface were characterized under mechanical tensile stress. Nanoparticle-enabled interfaces were observed to improve the interface bond between dissimilar materials, providing a method for improving the interface strength without altering the original material system. Based on these findings, nanoparticle-enabled diffusion control is shown to be a viable method for improving microstructural design and mechanical properties of multiphase materials.

ACKNOWLEDGMENTS

This thesis is supported by the National Science Foundation (NSF) award number: 1562543.

I would like to express my gratitude to Dr. Lianyi Chen, my advisor, for his guidance and patience during this process. I would also like to express gratitude to Dr. Charles Wojnar and Dr. Frank Liou for serving on the committee. Additionally, I would like to thank the research group for their assistance throughout the last two years. Any friends and acquaintances I have met during my time at Missouri University of Science and Technology produced an experience I certainly will not forget. Lastly, I would thank my entire family for their love and support.

TABLE OF CONTENTS

Page

LIST OF ILLUSTRATIONS

SECTION

1. INTRODUCTION

Metal-Matrix Nanocomposites (MMNCs), metals reinforced with nanoparticles (NPs), are well known to enhance material properties required for overcoming a wide range of engineering challenges. MMNC design typically focuses on dispersing NPs homogeneously throughout the matrix, with the NPs serving as the primary mechanism for enhancing material properties. In addition, NPs can also be used to control phase growth, offering additional mechanisms for improving the properties of existing material systems.

An extreme case highlighting the capabilities of controlling phase growth are immiscible alloys, which exhibit a liquid miscibility gap where the homogeneous liquid phase nucleates into two immiscible liquids before solidification. Due to the liquid miscibility gap, diffusion and convection based phenomena occur faster than solid-state phase transformations, preventing a uniform distribution of the secondary phase through conventional casting that has been used for the last hundred years.

Recently, NPs incorporated into an immiscible alloy produced a homogeneous distribution of the secondary phase during slow cooling [1]. NPs were characterized to restrict diffusional growth of minority droplets by rapidly assembling at the growing interface. The specific growth control mechanism, referred to as NP-enabled diffusion control, possesses immense potential for large scale manufacturing implementation by eliminating restrictions to sample size and processing times.

However, further characterization is required for advancing this new class of materials. This thesis is comprised of two journal papers focused on characterizing diffusion and mechanical properties of NP-enabled diffusion controlled materials. To quantify diffusion properties, NP-enabled diffusion control is characterized through *in-situ* high-energy

high-speed synchrotron X-ray imaging. Unlike previous *ex-situ* characterization of the final solidified microstructure, *in-situ* characterization allows the NP-enabled diffusion control mechanism to be observed during the phase transformation, and is capable of describing the exact behavior nanoparticles play in limiting droplet growth observed in the final microstructure. Through *in-situ* imaging of the melting process, NP-enabled alloys were characterized to limit diffusion of minority droplets to at least one order of magnitude slower than those in the pure alloy, providing direct evidence of this transient phenomena. For mechanical properties, NP-enabled interfaces observed under *ex-situ* microscopy of the final deformed microstructure were demonstrated to be effective in strengthening the interface compared to NP-absent interfaces. NP-enabled interfaces are shown to drastically alter the failure mechanism of minority droplets under an applied load. By coating the droplets with NPs, droplets were observed to fail from droplet fracture instead of interface decohesion, indicating that the interface was strengthened to levels beyond interface decohesion. These studies demonstrate the NP's effectiveness in enhancing both microstructural design and mechanical properties, and are instrumental for understanding property-structure relationships necessary to further advance NP-enabled diffusion controlled materials.

2. LITERATURE SURVEY

2.1. OVERVIEW OF IMMISCIBLE ALLOYS

Immiscible alloys, also known as monotectic alloys, are materials which exhibit a miscibility gap where the homogeneous liquid transforms into two immiscible liquids during solidification [1, 2]. Typical immiscible alloys such as Cu-Pb, Al-Pb, Al-Bi, Al-Id, and Zn-Bi have been investigated as potential high quality wear resistance materials, with the softer secondary phase lowering the coefficient of friction in applications such as self-lubricating load bearings [1–5]. However, a homogeneous distribution of minority phase is required and has been demonstrated to be difficult to achieve due to the miscibility gap.

Under equilibrium cooling of immiscible alloys, the minority phase initially nucleates into small liquid droplets homogeneously distributed throughout the melt. During cooling, in the miscibility gap, the small minority droplets experience diffusional growth, occurring orders of magnitude faster in liquids compared to solids. Additionally, the liquid droplets are free to migrate, coagulate, coalesce and Ostwald ripen, further increasing the droplet size and droplet-to-droplet spacing. Significant density mismatch, typical of immiscible alloys, induce sedimentation, causing the larger droplets to sink and eventually form a thick layer at the bottom of the crucible. Additionally, thermocapillary forces created by concentration gradients within the melt also act on the minority droplets, driving them radially towards the center of the melt pool, leading to collisions with other droplets.

With minority droplets experiencing a variety of forces and kinetic processes, immiscible alloys represent an extreme case of phase growth control, which is required to produce a homogeneous microstructure; discovering different methods for controlling immiscible alloys can also be adopted for improving other less problematic material systems.

2.2. IMMISCIBLE ALLOY DESIGN

Many processing solutions have been proposed to produce feasible immiscible alloys for practical applications. Rapid solidification has been applied to immiscible alloys to limit phase growth time and droplet transport during the miscibility gap. But at the same time, high temperature gradients experienced within the melt can reduce homogeneity through induced thermocapillary forces acting on the droplets [6, 7]. Casting in microgravity environments can eliminate sedimentation, improving homogeneity parallel to gravity, but not dispersed radially due to thermocapillary forces [7]. Thermoelectric magnetic forces have been used to control melt flow and refine the distribution of minority droplets [8–10]. Mixed powders of individual alloy constituents processed through ball milling and sintering can result in sufficiently homogeneous densified microstructures by avoiding the miscibility gap. However, all the solutions presented here are limited to specific sample sizes and processing windows and cannot be applied to satisfy large-scale manufacturing operations.

For large-scale manufacturing with a wide range of processing conditions, dispersed NPs offers an innovative solution for limiting phase growth. NPs have been shown to serve as effective inoculates, behaving as heterogeneous nucleation sites for minority phases [11–13]. By reducing the nucleation barrier, additional droplets are allowed to nucleate, producing smaller droplets unaffected by gravitational and thermocapillary forces. NPs with lower thermal conductivity than the base metal can effectively remove the latent heat to encourage further inoculation [14]. Particulates distributed in the melt can also increase viscosity within the melt [15], restricting droplet coagulation within the melt pool [5]. Additionally, NPs ahead of the solidification front are capable of altering local temperature, supersaturation, and diffusion flux, all critical factors for influencing phase distribution and growth [14, 16].

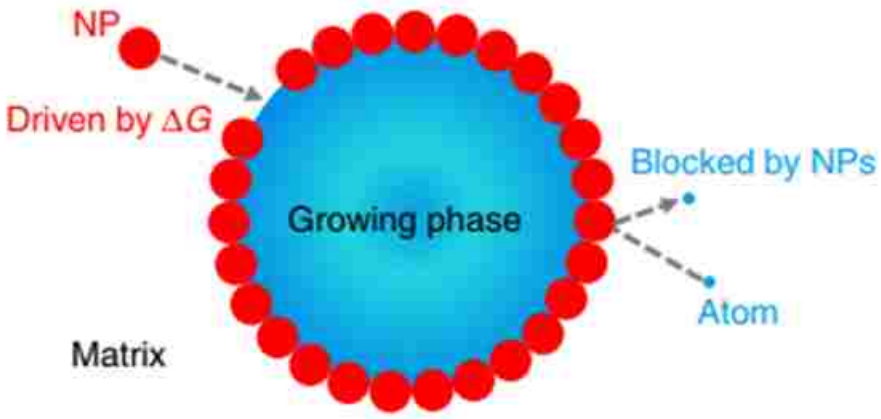

Figure 2.1. Schematic of NP-enabled diffusion growth control [1].

2.3. NANOPARTICLE-ENABLED DIFFUSION CONTROL

Recently, NPs present at the growing interface during slow solidification were determined to improve the homogeneity of immiscible alloys by limiting droplet size and motion [1, 4, 14]. For the microstructural refinement of the secondary phase achieved under slow cooling, the primary growth limiting mechanism was attributed to NPs physically blocking atomistic diffusion. By assembling and remaining at the growth interface during solidification, NPs can serve as physical barriers preventing additional solute atoms from diffusing into existing nucleated droplets as demonstrated in the schematic (Figure 2.1) and observed in the microstructure under scanning electron microscopy (SEM) (Figure 2.2(a)). The coated layer around the droplet (Figure 2.2(a)), zoomed into the interface (Figure 2.2(b)), was estimated to occur rapidly in approximately 4.4 ms based on the coated microstructure obtained at a cooling rate of approximately $11,340\ s^{-1}$ [1]. This cooling rate independent process has significant potential for large scale production, bypassing the limitations of processing times and sizes in current methods.

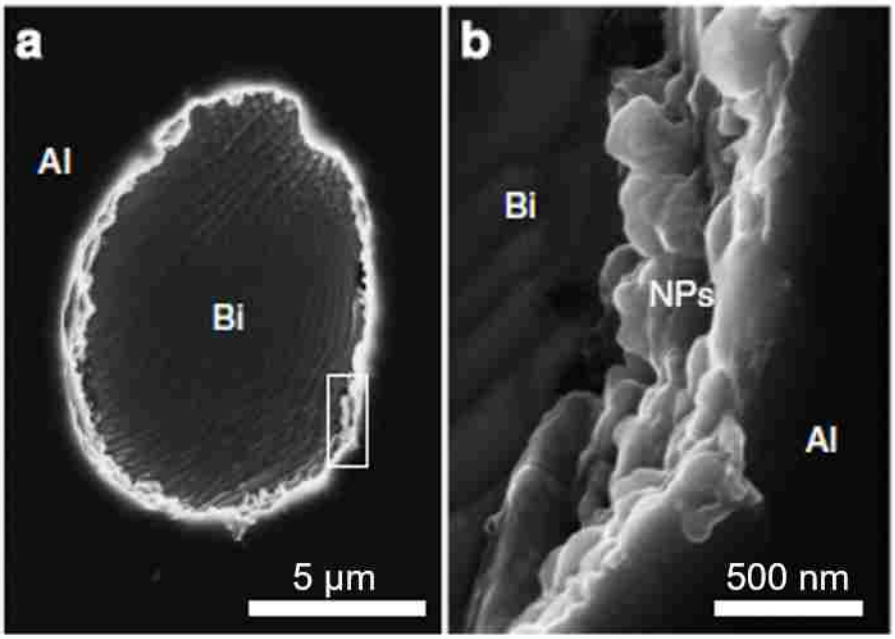

Figure 2.2. SEM image of a single droplet influenced by NP-enabled diffusion growth [1].

2.4. FABRICATION USING NANOPARTICLE-ENABLED DIFFUSION CONTROL

NP-enabled diffusion controlled materials are produced through ultrasonic-assisted casting based on the following technique [1]. Immiscible alloys are first heated into the homogeneous liquid phase L (Figure 2.3(a)). Then wettable NPs are distributed from the top of the melt pool until submerged. NPs are typically clustered with other NPs on gas bubbles within the melt due to strong intermolecular forces like van der Waals interactions.

To create a homogeneous distribution of NPs capable of coating the growing interface everywhere within the melt, ultrasonic cavitation is pulsated on the top of the meltpool. Ultrasonic cavitation (Figure 2.4) is used to break apart the agglomeration of NPs [17]. Cavitation occurs during expansion cycles by generating the sufficiently high pressures needed to overcome the tensile strength bonding of the liquid. While the strength of the liquid bond is generally higher than what most ultrasonic transducers can produce [18], trapped gas bubbles typically found in the liquid and in NP clusters serves as weak zones

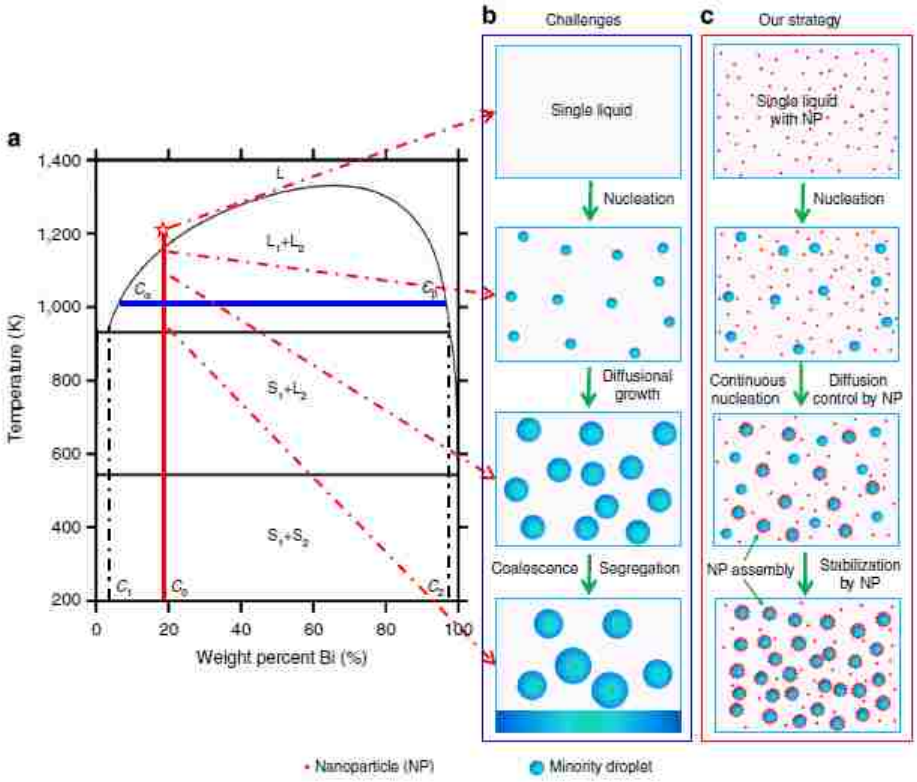

Figure 2.3. Methodology for controlling phase growth during solidification [1].

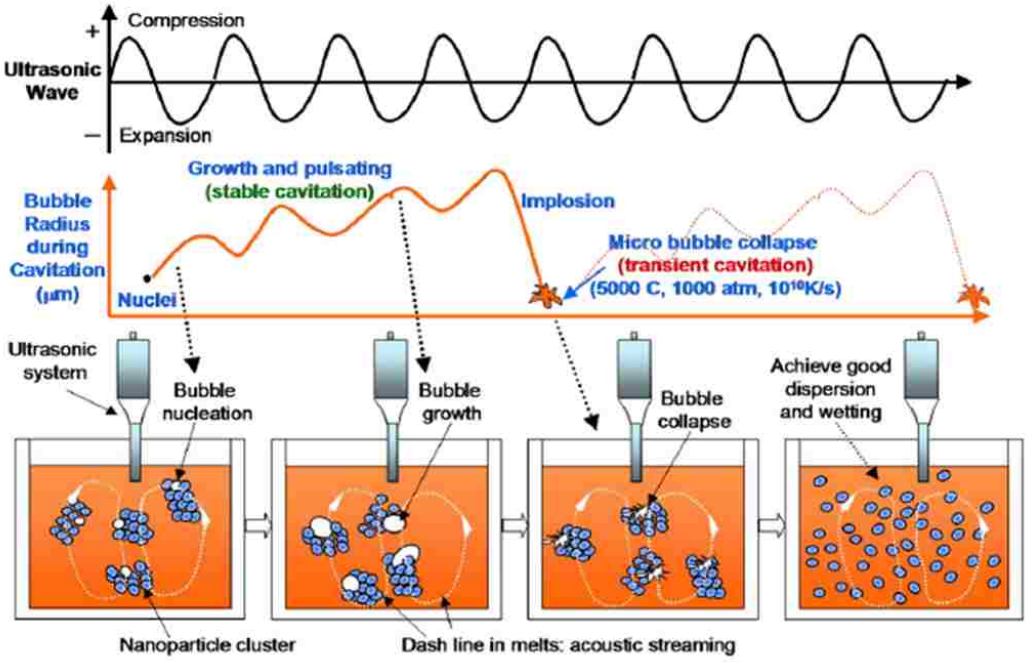

Figure 2.4. Uniform dispersion of NPs within liquid melt achieved through ultrasonic cavitation [1].

or nuclei where stress is concentrated. During compression, the cavities collapse, however, if high intensities are used during expansion, the cavities will not have time to react and will continue to grow until a critical radius is reached. This will cause the trapped gas to implode, generating "micro-hot spots," which can generate temperatures of 5000 °C, pressures above 1000 atm, and cooling rates above 10^{10} K/s. This process lasts on the order of pico-seconds and only affects a limited area [19]. The high shear stresses generated through the rapid collapse has been shown to break apart NP clusters, while dispersing them in the mold cavity through acoustic streaming generated by the probe vibrating the melt [17].

After dispersing NPs within the homogeneous liquid phase, the immiscible alloy is cooled, undergoing the following phase transformation: $L \rightarrow L_1 + L_2$ (Figure 2.3(a)). Subsequently, the dispersed NPs, will attempted to minimize their energy state by residing either in the majority phase L_1 (pink), minority phase L_2 (blue), or at the $L_1 - L_2$ interface.

For NP-enabled diffusion control, NPs are required to be thermodynamically to remain at the interface. Additionally, NPs must be chemically stable in the melt to remain solid in order to physically block diffusion growth of minority droplets. If NPs significantly favor the interface and are initially dispersed homogeneously, NPs will rapidly self-assemble at the interface immediately after the minority phase has nucleated. The energy required to keep the NPs at the liquid interface is equal to

$$\Delta G = \min\left[\pi r^2 \sigma \left(1 \pm \cos(\theta)\right)^2\right], \tag{2.1}$$

where r is the particle radius, σ is the interface free energy between the two liquids, θ is the contact angle, and '+' and '−' refer to the energy required to remove the particle into the bulk L_2 and L_1 phase, respectively. The interface free energy between the two liquids can be derived empirically through wetting experiments. For the aluminum-bismuth immiscible alloy (Al-Bi) specifically, the interface free energy can be related through temperature by [11]

$$\sigma = 288.1\left(1 - \frac{T}{1310\ \mathrm{K}}\right)^{1.26}\ \mathrm{mN\ m^{-1}}, \tag{2.2}$$

where T is the temperature in kelvins. Additionally, NPs may begin to slowly move away from the interface due to Brownian motion, with the energy,

$$E_b = \frac{kT}{2}, \tag{2.3}$$

where k is the Boltzmann constant. Due to the inherent weakness of Brownian energy, random NP motion only overcomes the interface energy for a short time after nucleation, allowing the NPs to reside at the interface during solidification.

With the NPs accumulating at the interfaces of freshly nucleated droplets (Figure 2.3(c)), additional solute is unable to diffuse into a coated droplet and is forced to nucleate elsewhere, limiting individual minority diffusion growth and Ostwald ripening. NP-coated

droplets are also unable to coalesce with other minority droplets during collisions. Without NPs, the freshly nucleated droplets experience unrestricted diffusion growth (Figure 2.3(b)). These larger droplets are prone to thermocapillary forces, further increasing the overall droplet size. Subsequently, sedimentation lowers the minority phase to the bottom of the crucible, forming a sedimented layer and concentration gradient of minority phase throughout the material. With NPs, the minority droplets are now homogeneously disperse within the melt and are too small to induce sedimentation or thermocapillary motion throughout the melt, improving the homogeneous dispersion of minority droplets from Figure 2.3(b) to Figure 2.3(c).

PAPER

I. *IN-SITU* OBSERVATION OF NANOPARTICLE-ENABLED DIFFUSION CONTROL BY HIGH-SPEED SYNCHROTRON X-RAY IMAGING

J. L. Volpe[1], Q. Guo[1,2], C. Zhao[3], L. H. Xiong[1], T. Sun[3], L. Y. Chen[1,2,a)]

[1] Department of Mechanical and Aerospace Engineering, Missouri University of Science and Technology, Rolla, Missouri 65409, USA

[2] Department of Materials Science and Engineering, Missouri University of Science and Technology, Rolla, Missouri 65409, USA

[3] Advanced Photon Source, Argonne National Laboratory, Argonne, Illinois 60439, USA

[a)]Corresponding author, email: chenliany@mst.edu

ABSTRACT

Nanoparticles assembled at the phase interface were recently hypothesized to control diffusion based on *ex-situ* characterization. However, the nanoparticle-enabled diffusion control mechanism has not been verified by *in-situ* evidence, because of the challenges with *in-situ* observation. In this study, the influence of nanoparticles assembled at the phase interface on diffusion is investigated through *in-situ* high-energy high-speed synchrotron X-ray imaging during laser melting of pre-cast alloys. Nanoparticles were observed to limit the calculated diffusion coefficient, based on a diffusion controlled model, by at least one order of magnitude compared to that of materials without nanoparticles. These findings provide *in-situ* evidence of nanoparticle-enabled diffusion control, which is essential for further advancing these new materials and manufacturing processes.

Keywords: Metal Matrix-NanoComposite, Immiscible alloy, Nanoparticle-enabled diffusion control, *In-situ* synchrotron X-ray imaging

Nanoparticles (NPs) have introduced innovative mechanisms for controlling phase growth during solidification [1–8]. Controlling phase growth is essential for achieving desired microstructures for enhancing material properties. Recently, NPs were discovered to refine phase domains by assembling at the phase interfaces (both solid-liquid and liquid-liquid interfaces) [1–3]. Based on *ex-situ* microscopy, NPs were hypothesized to control phase growth by physically blocking and stalling diffusional transport of solute atoms [1–3], referred to as NP-enabled diffusion control. However, *ex-situ* characterization cannot directly observe the transient microstructure evolution during solidification. Whether the NPs can effectively control diffusion during the solidification processing of metals is still a matter of debate. A deeper understanding and testing of NP-enabled diffusion control through *in-situ* characterization is essential for advancing NP-enabled diffusion control to applications beyond homogeneous microstructure design.

However, *in-situ* characterization of NP-enabled diffusion control entails a plethora of experimental challenges. Firstly, the NP-enabled inoculation [4–6] mechanism, where particles behave as heterogeneous nucleation sites for initiating phase domains/grains, is also capable of refining microstructures and will interfere with the observation of the NP-enabled diffusion control mechanism. Current *in-situ* characterization techniques are unable to observe the interaction of NPs with the newly formed phases, and are only able to observe the evolution of the newly formed phase during solidification. With both NP-enabled inoculation and NP-enabled diffusion control capable of influencing the phase morphology, accurately identifying the contribution of NP-enabled diffusion control on phase domain refinement is immensely difficult. Secondly, metals are not transparent to visible light. Observing inside the melt is extremely challenging by conventional characterization tools. Thirdly, phase domain growth and NP-enabled diffusion control happen very fast, within milliseconds [2].

To address these challenges, a unique experimental approach is designed. To overcome and avoid the interference from inoculation, pre-cast material melting, rather than it's solidification, is performed. However, melting of NPs pre-assembled at the interfaces introduces additional challenges. Conventional slow furnace heating may degrade the NP-coated interface during melting before dissolution occurs due to the long time effects of Brownian motion [9], potential chemical reaction, and Ostwald ripening [10, 11]. To reduce the extent of the NP coating degradation, rapid laser melting is performed to reduce the heating time. Melting of a pre-cast NP-coated minority phase will also ensure that NPs are initially present at the interface and are not initially dispersed between minority droplets. To observe through metals and observe the fast dynamics of phase domain growth, we use high-energy high-speed synchrotron X-ray imaging.

The experimental set-up for *in-situ* high-energy high-speed X-ray imaging during laser melting is shown in Figure 1. Thin plate specimens of the material were clamped between two glassy carbon plates, and encased in a stainless-steel chamber filled with argon. A continuous wave fiber laser with a wave length of 1070 nm (IPG) was used to melt the thin plate specimen, and was operated at 500 W with a focal spot diameter of 300 μm. The top surface of the thin plates were heated and melted by the laser for 4 ms. A series of images obtained by the X-ray penetrating through the melt pool were acquired at a rate of 54.31 kHz through a viewing window of 1024 μm $\times$ 1024 μm during laser melting.

Al-Bi immiscible alloys with and without $TiC_{0.70}N_{0.30}$ NPs (average diameter of approximately 80 nm), with similar initial Bi droplet morphologies, were used to analyze diffusion. The specimens suitable for *in-situ* characterization of NP-enabled diffusion control were prepared by ultrasonic processing. Ingots of Al-20wt.%Bi and Al-20wt.%Bi with 2 vol.% $TiC_{0.70}N_{0.30}$ NPs (also referred to as the pure and NP-enabled alloys, respectively) were melted in an alumina crucible, processed by ultrasonic processing, and then cooled to room temperature inside the furnace with a cooling rate of about 1 K/s. The details of

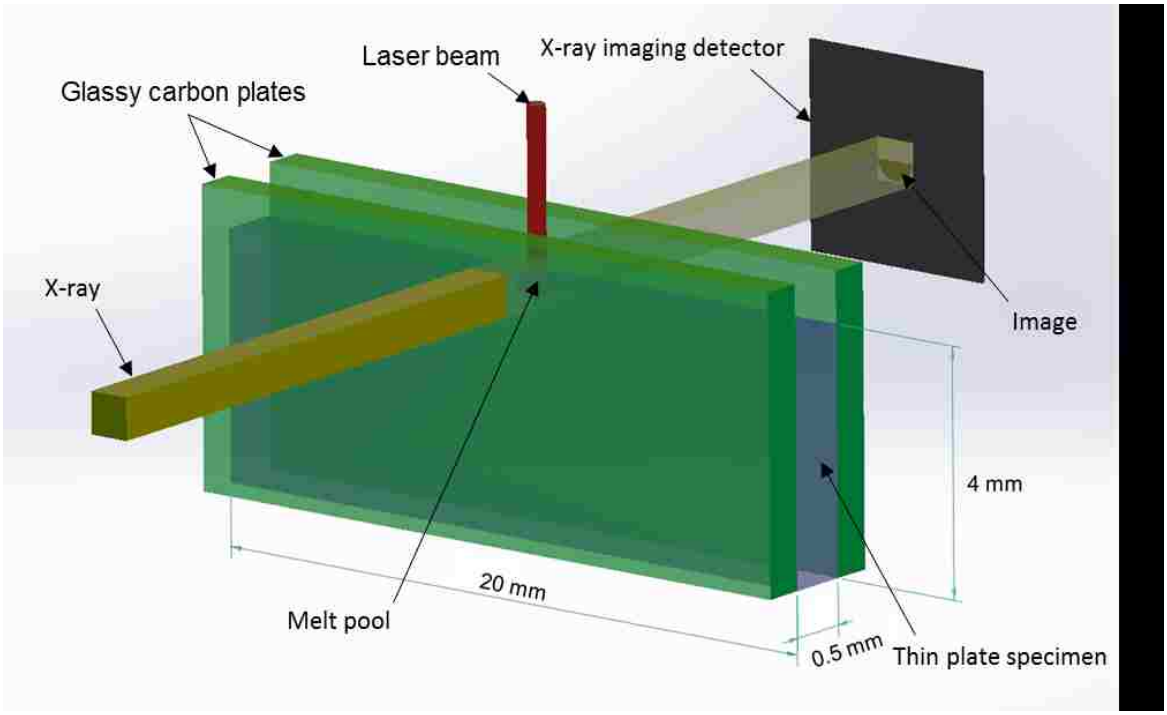

FIG. 1. Schematic of the *in-situ* characterization experimental set-up used to observe NP-enabled diffusion control. The thin plate specimen of the material, held between two glassy carbon plates, is heated by a laser beam with a diameter of 300 μm for 4 ms. The microstructure evolution during laser melting is characterized by high-energy high-speed x-ray imaging with a frame rate of 54.31 kHz. Figure is not to scale for visual clarity.

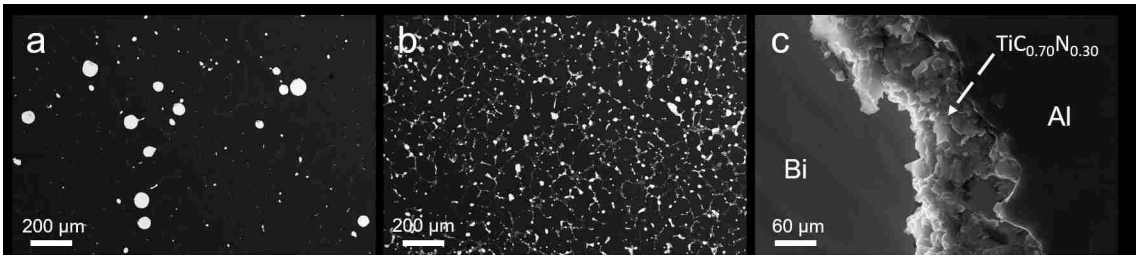

FIG. 2. Backscatter SEM images of Al-20wt.%Bi (remeasured to Al-4.2wt.%Bi) (a) and Al-20wt.%Bi with 2vol.% $TiC_{0.70}N_{0.30}$ NPs (b) initial microstructure taken from the center of the ingot. (c) High magnification SEM image showing the $TiC_{0.70}N_{0.30}$ particles assembled at the phase interface.

ultrasonic processing are described in the reference [2] Once solidified, thin plates were cut perpendicular to the base from the middle of the ingot and grinded into dimensions of 4 mm $\times$ 20 mm $\times$ 0.5 mm.

Before *in-situ* characterization, *ex-situ* microscopy was performed to determine the distribution of NPs and Bi droplets prior to *in-situ* laser melting. The Al-Bi microstructure without NPs is shown in Figure 2(a). Sedimentation (not shown in Figure 2(a)), significantly lowered the Bi composition within the center of the ingot. The composition was remeasured to be Al-4.2wt.%Bi determined by electron backscatter imaging. Figure 2(b) shows the NP-enabled microstructure with the addition of $TiC_{0.70}N_{0.30}$ NPs. Figure 2(c) is a zoomed-in image of Figure 2(b), which shows the NPs assembled at the Al-Bi interface.

From high-energy high-speed *in-situ* synchrotron X-ray imaging, the dissolution of a single minority droplet is shown in Figure 3(a-d) for the pure alloy and Figure 3(e-h) for the NP-enabled alloy. Bi droplets throughout different parts of the melt pool dissolved at non-constant rates as the melting front proceeded into the thin plate. To evaluate the diffusion properties, minority droplet size, droplet position, and the time required for the droplets to completely dissolve were obtained from the images. Complete dissolution of the liquid minority droplets based on the initial diameter of the minority droplet were solely considered due to thermocapillary forces elongating droplets into irregular shapes during

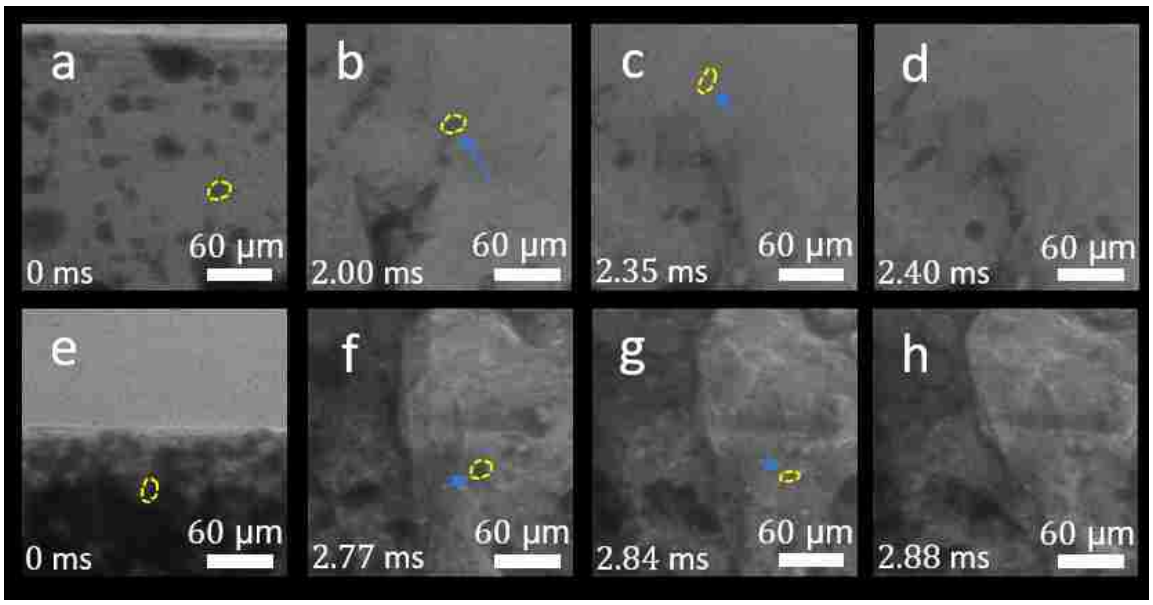

FIG. 3. Dissolution of a single minority phase under laser-induced melting conditions in pure (a-d) and NP-enabled (e-h) alloy. The dotted line represents one specified minority droplet. The arrow represents the motion of the specified minority droplet until complete dissolution.

melting. Using ImageJ (National Institutes of Health, version 1.51q), the average diameters and positions of minority droplets were carefully measured and averaged. The change in dissolution time of an individual droplet was estimated to begin when a slight change in droplet shape was observed, and ended when the droplet completely disappeared. Two and four melting experiments of the pure and NP-enabled alloys were recorded, respectively. Five minority phase droplets per experiment were examined, which also exhibited minimal non-diffusional behavior such as droplet collisions, droplet splitting, and droplet-pore interaction.

The following equation [12, 13] derived for diffusion-controlled dissolution was used to calculate the diffusion coefficient D of a single spherical droplet,

$$R = R_0 - \frac{SDt}{R_0} - \frac{2S}{\sqrt{\pi}}\sqrt{Dt}, \tag{1}$$

where R_0 and R are the initial radius and final radius, respectively, t the dissolution time, and S the supersaturation. Since the temperature of the melt pool changes during heating, an average supersaturation between the miscibility gap was used, and calculated based on the equilibrium phase diagram using the following equation,

$$S = \frac{1}{2}\frac{(C_0 - C_1)}{(C_2 - C_0)}, \tag{2}$$

where C_0 is the concentration of the minority phase, and C_1 and C_2 are the concentration of majority-rich and minority-rich liquid at monotectic temperatures, respectively. The value of S accounts for the differences in the equilibrium alloy composition and was calculated to be 0.0013 and 0.032 for the pure and NP-enabled alloys, respectively.

Based on the diffusion controlled dissolution equation, the diffusion coefficient calculated from each minority droplet are shown in Figure 4(a). The calculated diffusion coefficients are on the order of 10^{-4} to 10^{-5} m^2/s and 10^{-5} to 10^{-7} m^2/s for pure and NP-enabled alloys, respectively. A reduction of at least one order of magnitude is observed with the presence of the NPs at the interface, which is consistent for similar sized minority droplets under identical melting conditions. Even with convective transport present in immiscible alloys [14], an order of magnitude difference in calculated diffusion coefficients was still observed regardless of average droplet velocities, as shown in Figure 4(b). Significant variation among calculated diffusion coefficients for similar-sized droplets was observed as each Bi droplets were measured at different times and locations throughout the melt pool life span.

While a reduction of at least one order of magnitude was observed in the calculated diffusion coefficient, previous *ex-situ* analysis on the same alloy system predicted a reduction of the calculated diffusion coefficients much larger than one order of magnitude [2]. However, the calculated diffusion coefficients for this *in-situ* characterization represent only

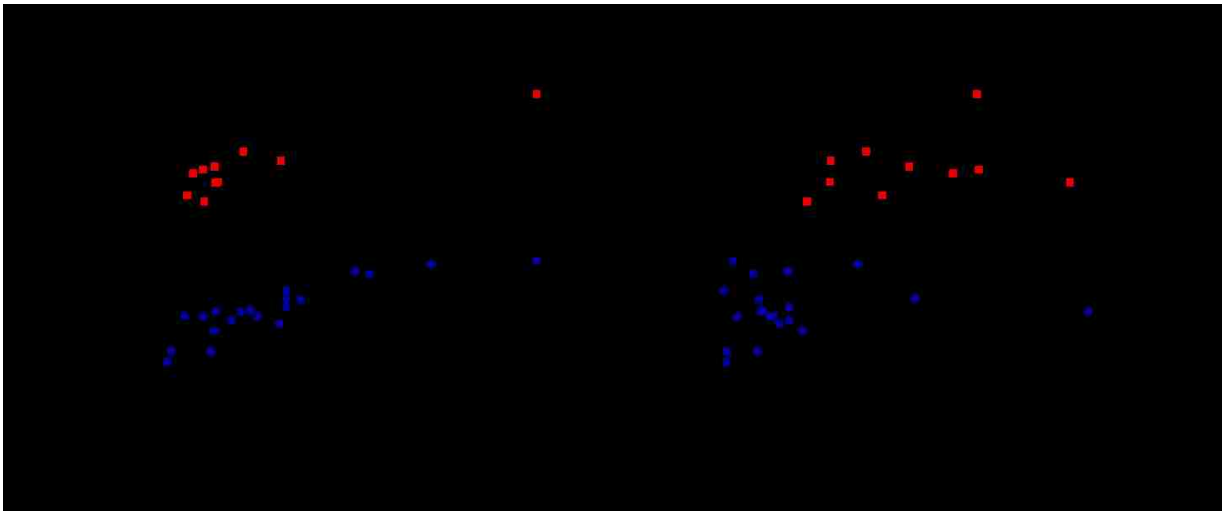

FIG. 4. (a) Calculated diffusion coefficient of pure and NP-enabled alloys for different sized Bi droplets. (b) Calculated diffusion coefficient of pure and NP-enabled alloys with different minority droplet velocities within the melt pool.

a conservative underestimation of the order of magnitude reduction. The high temperatures experienced during rapid melting may remove the NPs from the interface due to Brownian motion, rendering the NPs ineffective in physically blocking atomistic diffusion.

Despite the laser melting overcoming the experimental challenges essential to analyzing NP-enabled diffusion control, the calculated liquid diffusion coefficients of both alloys were significantly higher than typical liquid diffusion coefficients on the order of 10^{-8} to 10^{-9} m^2/s reported in literature [2, 14]. One possible explanation for the fast calculated diffusion coefficients observed during laser melting may be attributed to individual minority droplet's local concentration being inconsistent with the equilibrium concentration as assumed in equation 2. Under rapid melting conditions, the local minority concentration at the dissoluting minority droplets may be much greater than the equilibrium concentration as the high melting rate provides insufficient time for minority atoms to diffuse into equilibrium concentrations. A local minority concentration enrichment around minority droplets will reflect a higher local supersaturation than the equilibrium supersaturation. Unable to quantify the local droplet supersaturation, the underestimated equilibrium supersaturation

used in equation 1 will overestimate the calculated diffusion coefficients with the spatial and temporal measurements obtained through *in-situ* imaging. Accounting for the local supersaturation may lower the calculated diffusion coefficients to standard liquid diffusion coefficients and may yield an even larger order of magnitude difference than calculated with the equilibrium supersaturation. However, despite this discrepancy, at least one order of magnitude difference in the calculated diffusion coefficients was still characterized *in-situ* under similar melting conditions and using equilibrium concentrations.

With a one order of magnitude reduction in the calculated diffusion coefficient observed *in-situ*, NPs are shown to possess diffusion controlling properties. The primary mechanism for NP-enabled diffusion control is the NP's ability to stabilize at the phase interface during dissolution. As the Bi droplets dissolve, the NPs adsorb on the interface are able to physical restrict the flux of Bi atoms from crossing into the homogeneous liquid phase [2]. Additionally, nanochannels formed by the incomplete stacking structure of circular NPs assembled at the interface and by the Brownian motion of NPs crossing the interface can also stall the diffusion transport of Bi atoms [15].

In conclusion, NP-enabled diffusion control is characterized *in-situ* for the first time. Through *in-situ* high-energy high-speed synchrotron x-ray imaging of laser melting pure and NP-enabled alloys, dissolution of NP-coated and uncoated liquid-liquid interfaces were characterized. The calculated diffusion coefficients based on a diffusion based dissolution model were shown to restrict diffusion by at least one order of magnitude when NPs were assembled at the interface compared to when NPs were not used. This study overcomes many difficult experimental challenges to provide direct *in-situ* evidence of NP-enabled diffusion control. With diffusion underlying the physical phenomena in many fields [16–21], such as material science, biology, chemistry, and physics, validation of NP-enabled diffusion control through *in-situ* characterization is critical for further development in effective diffusion control.

ACKNOWLEDGMENTS

This work is supported by the National Science Foundation (NSF) award number: 1562543.

REFERENCES

[1] L.-Y. Chen, J.-Q. Xu, X.-C. Li, Mater. Res. Lett. 3 (2015) 43–49.

[2] L.-Y. Chen, J.-Q. Xu, H. Choi, H. Konishi, S. Jin, X.-C. Li, Nat. Commun. 5 (2014) 3879.

[3] C. Cao, L. Chen, J. Xu, J. Zhao, M. Pozuelo, X. Li, Mater. Lett. 174 (2016) 213–216.

[4] I. Kaban, M. Köhler, L. Ratke, W. Hoyer, N. Mattern, J. Eckert, A. L. Greer, Acta Mater. 59 (2011) 6880–6889.

[5] Q. Sun, H. Jiang, J. Zhao, J. He, Acta Mater. 129 (2017) 321–330.

[6] A. L. Greer, J. Chem. Phys. 145 (2016) 211704.

[7] T. T. Debela, X. D. Wang, Q. P. Cao, D. X. Zhang, J. J. Zhu, J. Z. Jiang, J. Appl. Phys. 117 (2015) 114905.

[8] K. Zhang, X. Bian, Y. Li, C. Yang, H. Yang, Y. Zhang, J. Alloys Compd. 59 (2015) 6880–6889.

[9] J. Q. Xu, L. Y. Chen, H. Choi, X. C. Li, J. Phys. Condens. Matter 24 (2012) 255304.

[10] A. Kabalnov, J. Dispers. Sci. Technol. 22 (2001) 1–12.

[11] E. E. Michaelides, Int. J. Heat Mass Transf. 81 (2015) 179–187.

[12] G. Thomas, M. Whelan, Philos. Mag. 6 (1961) 1103–1114.

[13] M. J. Whelan, Met. Sci. J. 3 (1969) 95–97.

[14] L. Ratke, S. Diefenbach, Mater. Sci. Eng. R (1995) 263–347.

[15] N. F. Y. Durand, A. Bertsch, M. Todorova, P. Renaud, Appl. Phys. Lett. 91 (2007) 203106.

[16] R. H. Tunuguntla, R. Y. Henley, Y.-C. Yao, T. A. Pham, M. Wanunu, A. Noy, Science 357 (2017) 792–796.

[17] J. C. S. Remi, A. Lauerer, C. Chmelik, I. Vandendael, H. Terryn, G. V. Baron, J. F. M. Denayer, J. Kärger, Nature Mater. 15 (2015) 401–406.

[18] P. Gruner, B. Riechers, B. Semin, J. Lim, A. Johnston, K. Short, J.-C. Baret, Nat. Commum. (2016) 10392.

[19] J. Feng, J. K. Nunes, S. Shin, J. Yan, Y. L. Kong, R. K. Prud'Homme, L. N. Arnaudov, S. D. Stoyanov, H. A. Stone, Adv. Mater. 28 (2016) 4047–4052.

[20] D. Luo, F. Wang, J. Zhu, F. Cao, Y. Liu, X. Li, R. C. Willson, Z. Yang, C.-W. Chu, Z. Ren, Proc. Natl. Acad. Sci. U.S.A. 113 (2016) 7711–7716.

[21] Y. Lu, Q. Hu, Y. Lin, D. B. Pacardo, C. Wang, W. Sun, F. S. Ligler, M. D. Dickey, Z. Gu, Nat. Commum. 6 (2015) 10066.

II. INTERFACIAL STRENGTHENING OF NANOPARTICLE-ENABLED INTERFACES

J. L. Volpe[1], Q. Guo[1,2], L. Xiong[1], L. I. Escano[1], L. Y. Chen[1,2,*]

[1] Department of Mechanical and Aerospace Engineering, Missouri University of Science and Technology, Rolla, Missouri 65409, USA

[2] Department of Materials Science and Engineering, Missouri University of Science and Technology, Rolla, Missouri 65409, USA

*Corresponding author, email: chenliany@mst.edu

ABSTRACT

Properties of dissimilar material systems are generally limited by their inherent interface. Weak phase interfaces, observed in dispersion strengthened materials, under external stresses can behave as initiation sites for void growth, leading to premature failure. Material systems prone to interface decohesion are generally avoided, forcing material scientists to select materials with inherently stronger interfaces, constraining the overall material selection design. To overcome this design limitation, nanoparticles were assembled at the phase interface. Nanoparticle-enabled interfaces under tensile testing conditions were characterized to strengthen the interface, and were able to change the overall secondary phase failure mechanism from interface decohesion to particle fracture. Nanoparticles are shown to increase the overall contact area at the interface, creating stronger and additional bonds between dissimilar materials. Furthermore, nanoparticle-enabled interfaces provide a method for improving the strength of dissimilar interfaces, without compromising the original material system.

Keywords: Metal Matrix-NanoComposite, Immiscible alloy, Nanoparticles, Interface strengthening

Interface strength between dissimilar materials can dictate overall material properties [1–9]. Interfaces are generally the weakest link in dissimilar materials systems, typically behaving as an initiation sites for void growth. Despite these weaknesses, solid interface bonds present in alloys, layered structures, welds, and composite materials have drastically surpassed standard monolithic properties. However, advances in dissimilar materials systems bypass improving the interface, instead focusing more on improving systems with inherently strong interfaces. The lack of improvement on material systems with inherently poor interfaces severely restrict certain material design combinations, especially in dispersed secondary phase alloys and composites.

Improving interfacial properties can be very challenging due to the lack of reliable testing methods of solid-solid interface energy [10]. While hardening the matrix can be used to prevent interface decohesion and strengthen the overall material, significant ductility is lost [11] and requires altering the original material system.

To enhance dissimilar interfaces, intermediate phases favorable to both materials have been shown to strengthen interfaces without compromising the original material system. Interlayers between two dissimilar materials during laser welding were observed to increase the overall strength of joint welds by suppressing the formation of certain intermetallic compounds [12]. Nanoscale transition layers improved the bonding of immiscible systems by producing a semi-coherent atomic structure [13]. Laminated structures utilizing hard brittle phases by stacking ductile metal thin sheets between layers has also been implemented to prolong ductility [14].

Additionally, improving interface strength through nanoparticles (NPs) also offers a novel solution to enhancing dispersed secondary phase interface properties. NPs inserted between accumulative roll bonded layers were shown to strengthen the layer interface [15]. Metallic NPs with organic residuals annealed between a double cantilever beam can greatly increase the interface fracture strength [16].

Recently, NPs were used to physically block and stall the diffusional transport of the minority phase in liquid immiscible alloys during nucleation by rapid assembling on the growing interface, forming a layer of NPs around the secondary phase, referred to as NP-enabled interfaces [17–19]. NPs energetically driven to specific interfaces upon solidification introduce a possible mechanism for interface strengthening, where the bonds between the phases and NPs may potentially be stronger than the bonds between the phases alone.

To determine whether NPs are capable of strengthening the interface, tensile testing of materials with and without NP-enabled interfaces are performed. The NP's influence on the interface and mechanical behavior of dispersed secondary phase is observed and compared to pure (NP-absent) interfaces. Here, NP-enabled interfaces are characterized to improve the interface strength between dissimilar materials.

To characterized NP-enabled interfaces, Al-Bi immiscible alloys with and without NPs were synthesized for mechanical testing using the following technique [17]. Al-20wt.%Bi alloys were melted into the homogeneous liquid phase region in a resistance furnace under an argon flux. For the NP-enabled alloy, two-volume percent of $TiC_{0.70}N_{0.30}$ NPs (average diameter of approximately 80 nm) were dispensed into the melt from the surface using a double capsulate feeding method [17]. Ultrasonic cavitation was subsequently used to break up NP clusters and achieve a homogeneous distribution of NPs within the melt before cooling. NPs nor ultrasonic treatment were used for the fabrication of the pure alloy. Both samples were cooled very slowly by removing the crucibles out of the furnace and into the air atmosphere. Ingots of Al-20wt.%Bi and Al-20wt.%Bi with 2vol.% $TiC_{0.70}N_{0.30}$ NPs (referred to as the pure and NP-enabled alloy, respectively) were cut by wire electrical discharge machining (EDM) into tensile bars with a length of 10 mm. Both tensile specimens were taken from the same height in the center of the ingot. The pure alloy composition was remeasured using electron backscatter imaging to Al-4.2wt.%Bi in the center of the ingot to account for sedimentation due to Al-Bi density mismatch. While the NP-enabled alloy had

no sedimentation, both materials had the same initial droplet nucleation morphology prior to NPs assembling at the interface. Tensile testing (Shimazu AGS-20kNG) was performed for the pure and NP-enabled alloys at a strain rate of $0.001s^{-1}$. Droplet interfaces were observed using a field emission scanning electron microscope (FESEM Zeiss LEO 1530).

Figure 1 shows the final deformed microstructure of the pure and NP-enabled alloy tensile specimens. Tensile loading for both alloys were applied parallel to the vertical direction of the image. The pure alloy (Figure 1(a)) shows significant inhomogeneity of Bi phase throughout the length of the tensile bar compared to the NP-enabled alloy (Figure 1(b)). The pure and NP-enabled samples failed at 0.12 and 0.10 strain, respectively. The NP-enabled alloy contains a far greater concentration of Bi phase, despite both samples being extracted from similar heights of their respective ingot. For the NP-enabled alloy, a partial coating of NPs were observed on many Bi droplets.

To compare the interface properties, two similarly sized droplets from each material were specifically analyzed (Figure 2). Droplets with complete coating in the NP-enabled alloy were solely analyzed. For the pure alloy, the Bi droplet experienced interface decohesion (Figure 2(a)). Comparatively, the NP-enabled droplet (Figure 2(b)) observed droplet fracture under a similar strain level. Additionally, the NP-enabled droplet also observed interface decohesion to a lesser degree compared to the pure droplet. The freshly separated interfaces for both droplets are shown in Figure 3. The droplet of the pure alloy is smooth (Figure 3(a)), compared to the rough surface of NPs embedded on the coated droplet (Figure 3(b)).

With casting of the pure alloy containing 20% Bi distributed homogeneously within the center ingot difficult due to sedimentation, a direct comparison between the NP-enabled alloy under tensile stress makes analyzing NP-enabled interfaces difficult. Nonetheless, the drastic differences in mechanical failure behavior between the NP-enabled and the pure alloy interfaces are significant for characterization. The SEM images of the final deformed droplets highlighted a change in the damage mechanism of the droplets, changing the overall

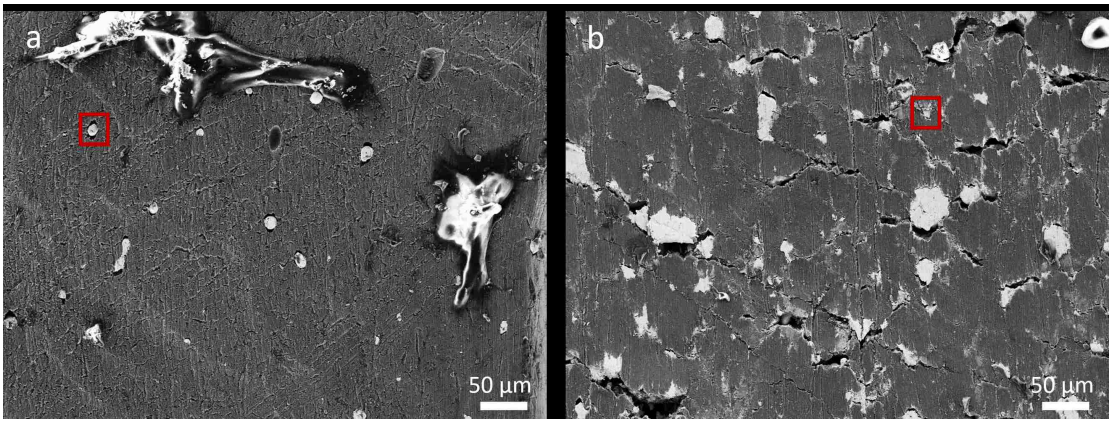

FIG. 1. SEM images of the final deformed microstructure of the pure (a) and NP-enabled (b) alloys. The NP-enabled alloy contained a greater concentration of Bi than the pure alloy due to sedimentation. Both samples were extracted at the same height of their respective ingots. Loading was applied in the vertical direction in the images. The red outline denotes a specific minority droplet examined in Figure 2.

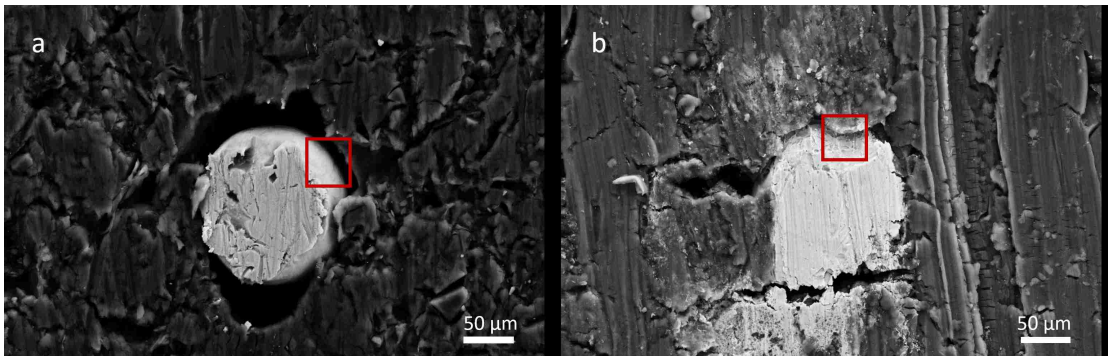

FIG. 2. SEM images of a specific similarly sized minority droplet from the pure (a) and NP-enabled (b) alloys outlined in red in Figure 1. Pure alloy droplets experienced interface decohesion, while the NP-enabled alloy experienced droplet fracture. The red outline denotes the specifc area of the interface examined in Figure 3.

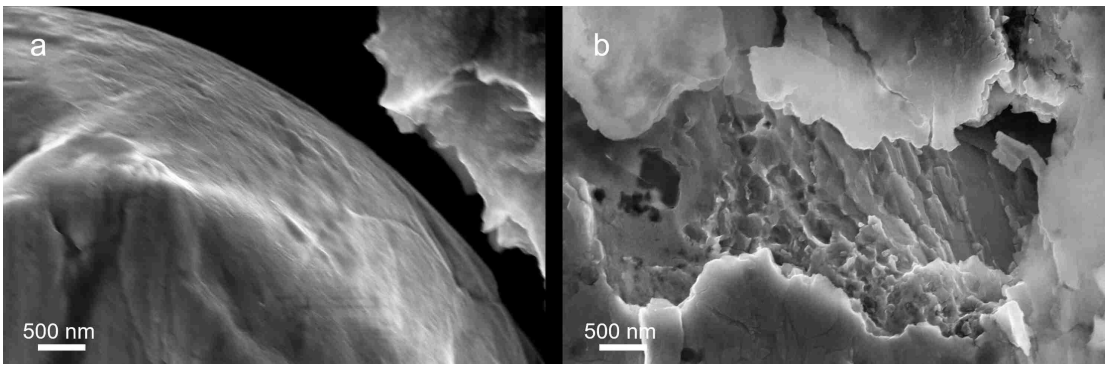

FIG. 3. SEM images of a freshly separated droplet surface from the pure (a) and NP-enabled (b) alloys droplet interface outlined in red in Figure 2. Pure alloy droplet surface was smooth, while the NP-enabled droplet had NPs embedded on the droplet.

failure method from interface decohesion in the pure alloy to droplet fracture in the NP-enabled alloy. This indicates that the NP-enabled interfaces increased the strength required for interface decohesion beyond the threshold required to initiate droplet fracture [11]. Failure within the droplet instead of at the interface demonstrates the interface is no longer the weakest link of this material system, which indicates the interface was strengthened. The increase in interface strength can be attributed to not only the strengthened chemical bonds formed between the intermediate NPs, but also a significant increase in the overall contact area for chemical bonding created through the rough NP coated layer (Figure 3). Beyond overcoming the stresses required to initiate interface decohesion, NPs also raised the stress required to induce particle fracture by impeding dislocation motion until even greater levels of stresses are achieved. Additionally, with Bi being softer and more brittle than Al, a high wt.% of Bi in Al-Bi is typically expected to exhibit less plasticity than a lower Bi concentration alloy. However, the NP-enabled alloy strain was similar to the strain of the pure alloy containing five times more Bi in terms of wt.% than the pure alloy, leading to the conclusion that NP-enabled interfaces increased the overall interface strength of the entire microstructure.

In conclusion, NP-enabled interfaces are shown to improve the interfaces between dissimilar materials. NP-enabled interfaces are observed to induce a change in droplet deformation behavior from interface decohesion in the pure alloy to droplet fracture in the NP-enabled alloy under tensile loading conditions. NPs are shown to strengthen the interface by strengthening the chemical bonds between each of the phases and by increasing the overall number of bonds through the increased contact area gained using NPs. Despite the NP-enabled alloys having five-times as much brittle phase compared to the pure alloy, similar levels of strain were observed in the pure alloys, which corresponds to the interfaces being strengthened throughout the microstructure. NP-enabled interface strengthening highlights a new way to strengthen material interfaces without altering the original material system.

ACKNOWLEDGMENTS

This work is supported by the National Science Foundation (NSF) award number: 1562543.

REFERENCES

[1] J. Howe, Int. Mater. Rev. 38 (1993) 233–256.

[2] J. Howe, Int. Mater. Rev. 38 (1993) 257–271.

[3] A. Mortensen, J. Llorca, Annu. Rev. Mater. Res 40 (2010) 243–270.

[4] N. Chawla, Y.-L. Shen, Advanced Engineering Materials 3 (2001) 357–370.

[5] P. J. Withers, M. Preuss, Annu. Rev. Mater. Res 42 (2012) 81–103.

[6] A. Pineau, A. A. Benzerga, T. Pardoen, Acta Mater. 107 (2016) 424–483.

[7] V. A. Romanova, R. R. Balokhonov, S. Schmauder, Acta Mater. 57 (2009) 97–107.

[8] E. Maire, V. Carmona, J. Courbon, W. Ludwig, Acta Mater. 55 (2007) 6806–6815.

[9] A. Weck, D. Wilkinson, E. Maire, A. Weck, D. Wilkinson, Mater. Sci. Eng.: A 448 (2008) 435–445.

[10] L. E. Murr, Mater. Sci. Eng. 12 (1973) 277–283.

[11] L. Babout, E. Maire, R. Fougères, Acta Mater. 52 (2004) 2475–2487.

[12] M. Gao, S. Mei, X. Li, X. Zeng, Scr. Mater. 67 (2012) 193–196.

[13] L. Liu, L. Xiao, J. Feng, L. Li, S. Esmaeili, Y. Zhou, Scr. Mater. 65 (2011) 982–985.

[14] G. Fan, L. Geng, H. Wu, K. Miao, X. Cui, H. Kang, T. Wang, H. Xie, T. Xiao, Scr. Mater. 135 (2017) 63–67.

[15] C. Lu, K. Tieu, D. Wexler, J. Mater. Process. Technol. 209 (2009) 4830–4834.

[16] I. Lee, S. Kim, J. Yun, I. Park, T.-S. Kim, Nanotechnology 23 (2012).

[17] L.-Y. Chen, J.-Q. Xu, H. Choi, H. Konishi, S. Jin, X.-C. Li, Nat. Commun. 5 (2014) 3879.

[18] L.-Y. Chen, J.-Q. Xu, X.-C. Li, Mater. Res. Lett. 3 (2015) 43–49.

[19] C. Cao, L. Chen, J. Xu, J. Zhao, M. Pozuelo, X. Li, Mater. Lett. 174 (2016) 213–216.

SECTION

3. CONCLUSIONS

Diffusion and mechanical properties of NP-enabled diffusion controlled materials were characterized. NP-enabled diffusion control was observed *in-situ* under high-energy high-speed synchrotron X-ray imaging, and was shown to reduced the diffusion coefficient by at least one order of magnitude. *In-situ* characterization showcases direct evidence of NP-enabled diffusion control, providing clarity to the conclusions obtained through *ex-situ* microscopy. The NPs assembled at the growing interface, in addition to blocking diffusion, were also characterized to improve interface strength. Based on *ex-situ* microscopy of the deformed microstructure, NPs were determined to strengthen the dissimilar material interfaces by improving the chemical bonds and increasing the overall contact area at the interface. With interfaces known to be the weakest part of the microstructure, behaving as initiation sites for void growth, strengthened NP-enabled interfaces were shown to change the failure behavior of minority droplets from interface decohesion to fracture, providing a general methodology for improving all material system interfaces. Both types of analyses provide validity to these microstructural refinement and interface strengthening strategies, which are necessary for continual advancement of this new class of materials.

REFERENCES

[1] L.-Y. Chen, J.-Q. Xu, H. Choi, H. Konishi, S. Jin, X.-C. Li, Nat. Commun. 5 (2014) 3879.

[2] L. Ratke, S. Diefenbach, Mater. Sci. Eng. R (1995) 263–347.

[3] B. Gollas, A. Luegger, J. Zidar, ECS Trans. 50 (2013) 123–133.

[4] C. Cao, L. Chen, J. Xu, J. Zhao, M. Pozuelo, X. Li, Mater. Lett. 174 (2016) 213–216.

[5] K. Zhang, X. Bian, Y. Li, C. Yang, H. Yang, Y. Zhang, J. Alloys Compd. 59 (2015) 6880–6889.

[6] C. P. Wang, X. Liu, I. Ohnuma, R. Kainuma, K. Ishida, Science 297 (2002) 990–993.

[7] T. Carlberg, H. Fredriksson, Metall. Trans. A 11A (1980) 1665–1676.

[8] Y. Zhong, T. Zheng, L. Dong, B. Zhou, W. Ren, J. Wang, Z. Ren, F. Debray, E. Beaugnon, H. Wang, Q. Wang, Y. Dai, Mater. Des. 100 (2016) 168–174.

[9] T. X. Zheng, Y. B. Zhong, Z. Lei, Z. M. Ren, F. Debray, E. Beaugnon, Y. Fautrelle, Mater. Des. 100 (2016) 168–174.

[10] H. Yasuda, I. Ohnaka, O. Kawakami, K. Ueno, K. Kishio, ISIJ Int. 42 (2003) 942–949.

[11] I. Kaban, M. Köhler, L. Ratke, W. Hoyer, N. Mattern, J. Eckert, A. L. Greer, Acta Mater. 59 (2011) 6880–6889.

[12] Q. Sun, H. Jiang, J. Zhao, J. He, Acta Mater. 129 (2017) 321–330.

[13] A. L. Greer, J. Chem. Phys. 145 (2016) 211704.

[14] L.-Y. Chen, J.-Q. Xu, X.-C. Li, Mater. Res. Lett. 3 (2015) 43–49.

[15] C. Ma, L. Chen, J. Xu, J. Zhao, X. Li, Journal of Applied Physics 117 (2015) 114901.

[16] B. F. Schultz, J. B. Ferguson, P. K. Rohatgi, Mater. Sci. Eng.: A 530 (2011) 87–97.

[17] Y. Yang, J. Lan, X. Li, Mater. Sci. Eng.: A 380 (2004) 378–383.

[18] K. S. Suslick, Sci. Am. 260 (1989) 80–86.

[19] G. I. Eskin, D. G. Eskin, Ultrasonic Treatment of Light Alloy Melts, 2 ed., CRC Press, 2015.

VITA

Joseph Louis Volpe was born in Saint Louis, Missouri. He received his B.S. in Mechanical Engineering from the Missouri University of Science and Technology in December, 2015.

During the course of his graduate study, he authored two papers for publication, which are contained in this thesis. In December 2017, he received his M.S. in Mechanical Engineering from the Missouri University of Science and Technology under the advisement of Dr. Lianyi Chen.